Pore structure controls stability and molecular flux in engineered protein cages

Lachlan Adamson[† 1,8], Nuren Tasneem[† 1], Michael P. Andreas[† 2,3], William Close[† 4], Taylor N. Szyszka [1], Eric Jenner [1], Reginald Young [1], Li Chen Cheah [6,8], Alexander Norman [1], Frank Sainsbury [6,7,8], Tobias W. Giessen* [2,3] and Yu Heng Lau* [1,5]

1. School of Chemistry, The University of Sydney, NSW 2006, Australia
2. Department of Biomedical Engineering, University of Michigan Medical School, Ann Arbor, MI, USA
3. Department of Biological Chemistry, University of Michigan Medical School, Ann Arbor, MI, USA
4. Australian Centre for Microscopy & Microanalysis, The University of Sydney, NSW 2006, Australia
5. The University of Sydney Nano Institute, The University of Sydney, NSW 2006, Australia
6. Australian Institute for Bioengineering and Nanotechnology, The University of Queensland, QLD 4072, Australia
7. Centre for Cell Factories and Biopolymers, Griffith Institute for Drug Discovery, Griffith University, QLD 4111, Australia
8. CSIRO Future Science Platform in Synthetic Biology, Commonwealth Scientific and Industrial Research Organisation (CSIRO), 41 Boggo Road, QLD 4102, Australia

† co-first authors

Abstract

Protein cages are a common architectural motif used by living organisms to compartmentalize and control biochemical reactions. While engineered protein cages have recently been featured in the construction of nanoreactors and synthetic organelles, relatively little is known about the underlying molecular parameters that govern cage stability and molecular flux through their pores. In this work, we systematically designed a 24-member library of protein cage variants based on the *T. maritima* encapsulin, each featuring pores of different size and charge. Twelve encapsulin pore variants were successfully assembled and purified, including eight designs with exceptional and prolonged thermal stability. Pores lined with anionic residues resulted in more robust assemblies than their corresponding cationic variants. We then determined seven cryo-EM structures of pore variants at resolutions between 2.5-3.6 Å. Together with stopped-flow kinetics experiments for quantifying cation influx, we uncover the complex interplay between pore size, charge, and flexibility that controls molecular flux in protein cages, providing guidance for future nanoreactor designs.

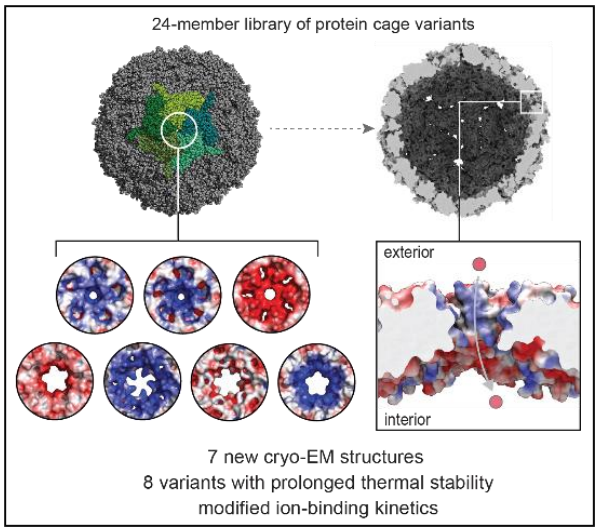

Introduction

Spatial organization is a fundamental principle used by Nature to coordinate the complex network of biochemical reactions necessary for life. In recent years, protein cages have emerged as a diverse and widespread architecture for organization in bacteria, alongside canonical lipid-bound organelles and phase-separated membraneless condensates.[1] An illustrative example of protein cage function is the carboxysome, a nanoscale compartment that

facilitates carbon fixation in cyanobacteria and other autotrophs.[2] The proteinaceous outer shell of a carboxysome is thought to function as a semi-permeable barrier, permitting influx of the substrate HCO_3^-, while retaining the volatile intermediate CO_2 and excluding the entry of cross-reactive O_2.[3–7] This control over molecular flux afforded by the outer cage is crucial for achieving optimal reaction kinetics.

Inspired by the carboxysome and other naturally-occurring protein cages, chemists and bioengineers have endeavoured to use modified and *de novo* protein cages as nanoreactors, hosting custom chemical reactions within their controlled internal environment.[8–14] Despite many efforts, the design of customizable nanoreactors remains in its infancy, as the impact of encapsulation on molecular flux is still poorly understood. Numerous groups have reported the successful encapsulation of enzymes within protein cages,[12,15–20] but these engineered cages have yet to emulate or surpass natural systems in terms of controlling substrate influx, co-factor retention, and product efflux. Seminal work by Tullman-Ercek and co-workers indicated the possibility of charge-based control, using anionic point mutations at the pores of MS2 bacteriophage capsid particles to slow the efflux of negatively charged species, based on modelling of experimentally-determined enzyme activity measurements.[21] In a complementary approach, Hilvert and co-workers designed lumazine synthase cages with a negatively-charged interior to bias the encapsulation of positively-charged species.[22] Meanwhile, Lutz and co-workers have instead reported pore size as a crucial determinant of molecular flux into encapsulin cages.[23] While these and other studies[24–27] suggest the tantalizing possibility of programmable molecular flux through a combination of size and charge, there has yet to be a systematic and comprehensive *in vitro* investigation into cage pore variants. Furthermore, insights into the impact of pore design have been limited by the lack of elucidated structures for pore-engineered cages in earlier studies.

In this work, we investigate the structure, stability, and porosity of engineered cages from a 24-member library covering different pore sizes and surface charge profiles, each based on the encapsulin protein from *T. maritima*.[28] Encapsulins are a family of prokaryotic protein organelles that self-assemble into virus-like capsid structures of icosahedral symmetry, with external diameters ranging from 24-42 nm depending on the species.[28–33] Our rationale for choosing encapsulins is their ability to form extremely robust and homogeneous cage assemblies from a single type of protein building block. Specifically, the *T. maritima* encapsulin features narrow 3 Å pores at the five-fold axes of symmetry lined by a flexible peptide loop that Lutz and co-workers have shown is amenable to mutation and deletion (Figure 1a).[23] The combination of robustness and engineerability has given rise to a growing number of literature reports where encapsulins have been used in biotechnological applications such as synthetic organelles, drug delivery, and vaccines.[12,34–39]

Herein, we systematically explore the impact of pore structure and charge on nanoreactor design. We test the integrity of a homogeneously purified encapsulin pore variant library using a combination of negative stain transmission electron microscopy (TEM), size-exclusion chromatography coupled to multi-angle light scattering (SEC-MALS), and thermal denaturation coupled to dynamic light scattering (DLS). We then characterize the size and surface electrostatics of our pore designs by determining structures of seven pore variants by single particle cryo-electron microscopy (cryo-EM), and quantify the kinetics of molecular influx using stopped-flow fluorescence spectroscopy in an established lanthanide binding tag (LBT) assay[23,40].

Results

Design and purification of charged pore variants

We designed 24 novel variants of the *T. maritima* encapsulin (**S1X-S7X** where X=D/E/K/R, Figure 1b) by introducing a combination of charged point mutations and deletions at the flexible loop lining the five-fold symmetrical pore. This pore region had previously been reported by *Williams et al.* to be partially tolerant to mutagenesis with alanine or glycine without completely compromising cage self-assembly.[23] To systematically explore the effects of positively and negatively charged substituents in tandem with pore-widening deletions, we incorporated aspartic acid, glutamic acid, lysine, and arginine as single, double, and triple point mutants (**S1-S3**), and as flanking positions adjacent to deletions of two, four, or seven residues (**S4-S7**). As a positive control, we also included a pore deletion flanked with glycine (**S7G**) that had previously been reported to increase molecular flux.[23]

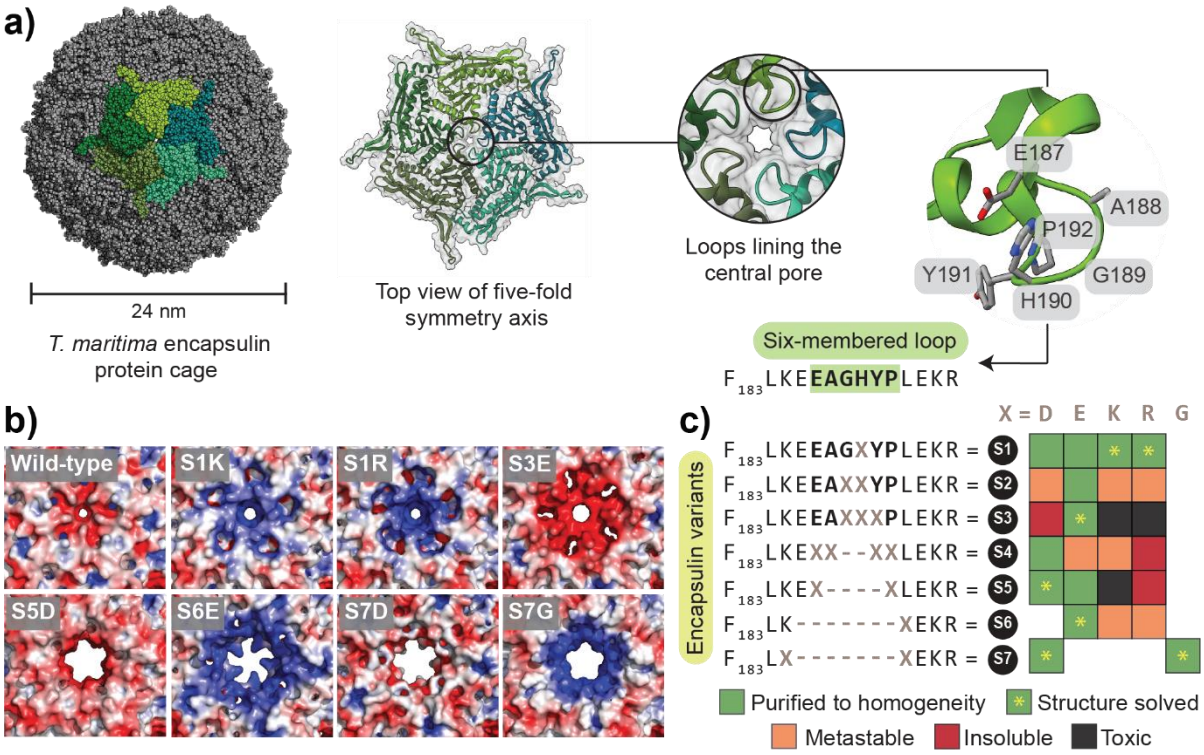

Figure 1. Sequence, structure and solubility of the encapsulin pore mutant library. a) The self-assembled hollow cage structure of the *T. maritima* encapsulin with an external diameter of 24 nm (structure from PDB 3DKT).[28] Top view shows the location of central pore at five-fold symmetry axis of *T. maritima* encapsulin, lined by peptide loops from each monomer (residues 187-192). **b)** Novel structures of seven encapsulin variants that we determined by cryo-EM, featuring diverse pore surface electrostatics that differ from the wild-type cage. **c)** Matrix displaying 24 encapsulin variants **S1X-S7X** we designed in this study, along with the **S7G** positive control,[23] indicating their sequence design and solubility post-expression and during purification. Metastable indicates precipitation during purification, while toxic indicates impaired growth of the expression host.

All encapsulin variants were recombinantly expressed in *E. coli* and subjected to a thorough multi-step purification protocol to obtain pure and monodisperse encapsulin assemblies. This protocol involved initial enrichment from cell lysate by precipitation with poly(ethylene)glycol followed by crude size-exclusion chromatography (SEC), ion-exchange chromatography (IEC) to remove surface-bound nucleic acids, and final polishing with two further rounds of SEC (SI Section 3).

Charge of pore residues governs robustness of cage assembly

Upon expressing each member of the encapsulin variant library, we found that eleven variants and the positive control could be expressed and purified to homogeneity (Figure 1c). An additional seven variants were metastable, eluting at the expected size in the first round of SEC, but precipitating irreversibly after fractionation or during subsequent purification steps. Of the remaining six variants, **S3D**, **S4R** and **S5R** were expressed in an insoluble form (SI Figure S3.1), while **S3K**, **S3R** and **S5K** resulted in toxicity for the expression host.

Negatively charged variants were clearly more capable of forming assembled cages than their corresponding positively charged variants. The only completely insoluble negatively charged variant was the aspartic acid triple point mutant **S3D**, possibly due to a combination of unfavorable charge repulsion and steric effects. Intriguingly, the analogous glutamic acid mutant **S3E** formed soluble assemblies, potentially due to the extra methylene unit allowing greater flexibility to relieve geometric and charge-repulsion constraints. In stark contrast, the only two positively charged variants that we could purify to homogeneity were the single point mutants **S1K** and **S1R**.

Assembled pore variants retain native structure and high thermal stability

All successfully purified assemblies retained a similar overall molecular architecture to that of the wild-type *T. maritima* encapsulin (Figure 2a; SI Section 4). Both TEM and DLS data showed that our purified samples were monodisperse, confirming the homogeneity of cage assembly. The expected diameter of 24 nm was observed for all assembled cages by TEM of negatively stained samples, with no evidence of aberrant assemblies (Figure 2ai; SI Figure S4.1). The hydrodynamic size of the cages in Tris buffer was measured by DLS and found to be consistent with the TEM data (Figure 2aii; SI Table S4.3). Purity and monodispersity were further confirmed by SEC-MALS, with a single peak observed for each purified variant (Figure 2aiii; SI Figure S4.2) giving an assembled mass of 2-2.5 MDa. SDS-PAGE analysis showed a clear band for the encapsulin monomer at the expected size of 33 kDa (Figure 2aiv; SI Figure S3.4).

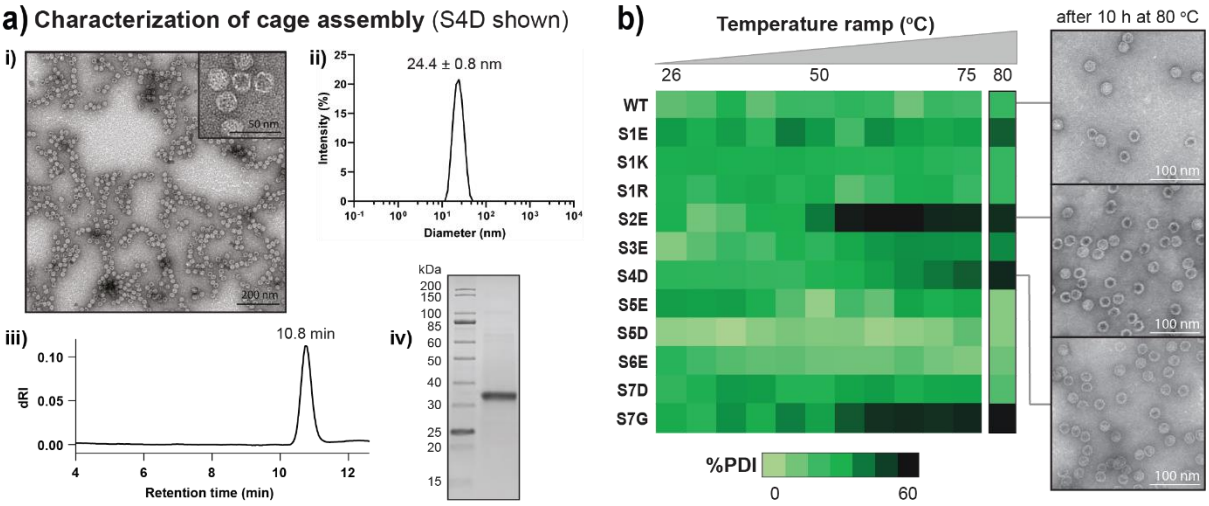

Figure 2. Pore variants can self-assemble and are stable at high temperatures. a) Exemplar characterization data for purified variant **S4D** (data for other variants can be found in SI Sections 3 and 4). (i) Negative stain TEM image of assembled cages. (ii) DLS profile showing the expected hydrodynamic size. (iii) Analytical SEC chromatogram (Bio SEC-5 1000 Å column) showing the presence of a single monodisperse species. (iv) SDS-PAGE analysis showing a single band corresponding to the encapsulin monomer. **b)** Heat map of the change in polydispersity index (%PDI) upon increase in temperature (from left to right: 26, 30, 36, 40, 44, 50, 56, 61, 66, 70 and 75 °C). TEM images of selected variants show the presence of intact assemblies after 10 h incubation at 80 °C.

Prolonged thermal stability was observed for all but two of the purified charged pore variants, revealing a remarkable degree of structural integrity and robustness to mutagenesis (Figure 2b). Upon heating samples to 75 °C while monitoring hydrodynamic size and polydispersity by DLS, we observed minimal changes in all charged pore variants except for **S2E** and to a lesser extent **S4D**, where we saw an increase in polydispersity that was irreversible upon cooling to 25 °C, indicative of aggregation or denaturation. A similar irreversible increase in polydispersity was observed for the glycine control variant **S7G**. A further overnight incubation of all samples at 80 °C yielded no significant changes. Despite the thermal instability of **S2E** and **S4D**, we still observed the presence of intact assemblies by negative stain TEM after prolonged heating, indicating that only partial denaturation or aggregation had occurred.

Cryo-EM structures display a range of pore sizes and surface electrostatics

We elucidated the atomic structures of seven selected pore variants by single particle cryo-EM (SI Figures S6.1 and S6.2), chosen to illustrate how our designed sequence modifications result in a diverse range of pore sizes and surface charge profiles (Figures 3 and 4). The structures for encapsulin cages containing point mutations (**S1R**/**S1K**/**S3E**), a partial loop deletion (**S5D**), and complete loop deletion (**S6E**/**S7D**/**S7G**), were determined at resolutions ranging from 2.5-3.6 Å. Further, all variants contained clear density for a tightly bound flavin-based molecule located close to the three-fold symmetry axis which had not been identified before for any T1 encapsulin (SI Figure S4.4). Pore channel dimensions were calculated based on the cryo-EM structures using the program HOLE,[41] while electrostatic surface potentials were calculated using the software APBS.[42]

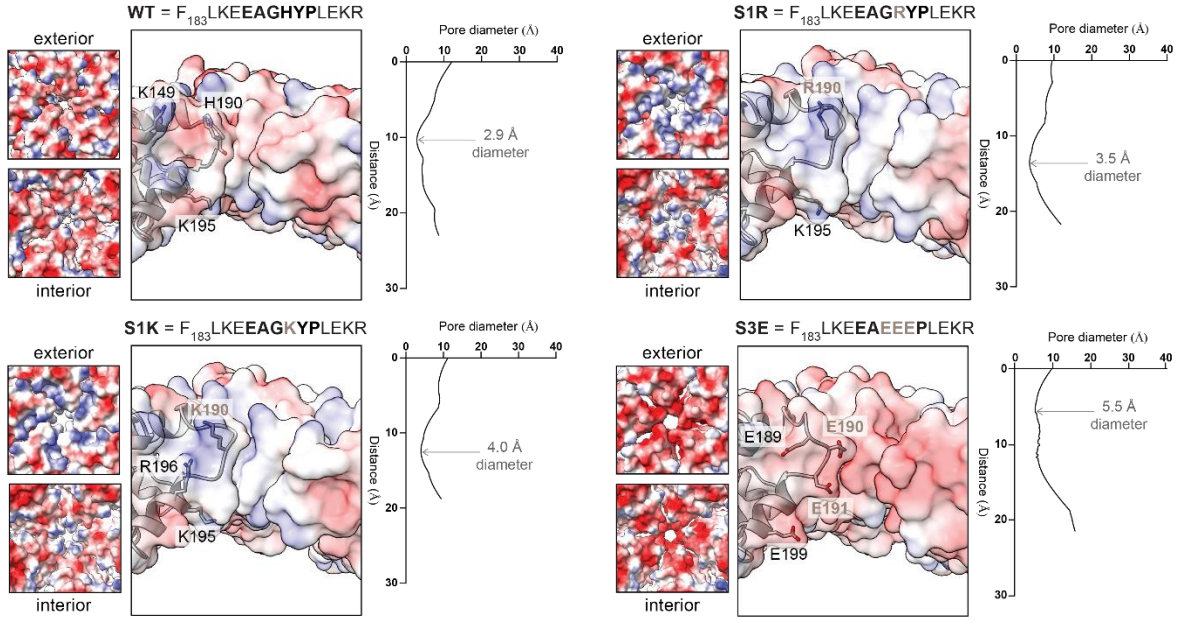

Figure 3: Cryo-EM structures of the pore channels from point mutation variants (S1R/S1K/S3E) show altered surface electrostatics. For each pore channel, the exterior and interior surface charge is shown, where red is negative and blue is positive. A cross-sectional view of each pore is also shown, presenting three of the five monomers at the five-fold symmetric pore. Each corresponding graph displays the pore size throughout the channel measured, indicating the narrowest point for each variant. Distance refers to the position along the pore axis from exterior to interior, while pore size is calculated using the program HOLE.[41] The wild-type structure is shown for comparison (PDB 3DKT).[28]

The single point mutants **S1R** and **S1K** retain similar pore dimensions in comparison to the wild-type, but a complete inversion of surface electrostatics is observed at the exterior entrance of the pore (Figure 3). The inversion to a positively charged entrance arises from the introduction of basic side-chain functional groups, together with subtle backbone conformational changes. In the wild-type encapsulin, the backbone carbonyl oxygen of H190 points directly into the pore, generating a negatively charged ring at the entrance of the pore. After mutation to R190 and K190, the peptide loop shifts outwards, such that the backbone carbonyl oxygen moves to point obliquely away from the pore lumen. No significant changes are observed on the positively charged interior surface lined by the side-chain of K195.

Major conformational shifts in the **S3E** variant results in strong negative charge throughout the pore channel and both entrances (Figure 3). The negative charge arises from E190 and E191, which line the external and internal entrances of the pore respectively as expected, while the carbonyl oxygen of E190 also points directly into the pore. The large 90° sideways shift in the pore loop conformation enables the increased steric bulk of the glutamate sidechains to be accommodated, resulting in an increase in overall pore diameter to 5.5 Å.

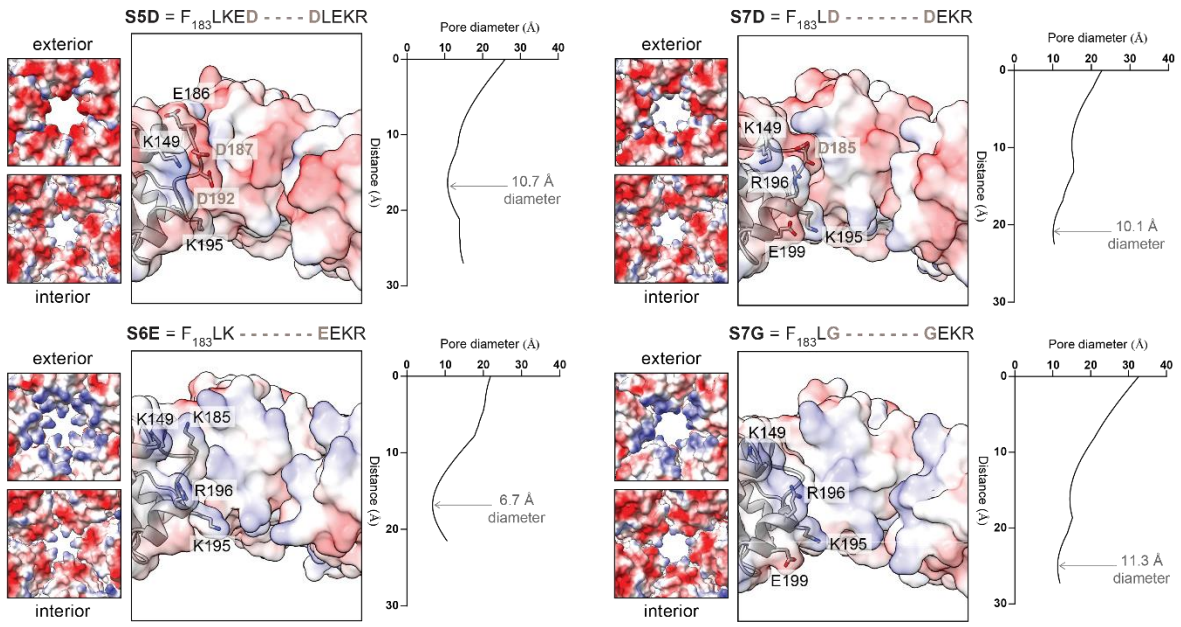

Figure 4: Cryo-EM structures of loop deletion variants (S5D/S6E/S7D/S7G) show a combination of widened pores and altered surface electrostatics. Residue numbering is kept consistent with wild-type to facilitate comparison.

The deletion variant **S5D** removes most of the pore loop, widening the pore to a diameter of 10.7 Å (Figure 4). The loop between the two helices leading to and away from the pore is replaced by a short pseudo-helical turn spanning residues 186/187/192/193 (residues 188-191 are deleted), with side-chain carboxylates of D187 and D188 pointing directly into the pore. The net result is a strongly negative pore channel and exterior entrance, while K195 continues to contribute some positive charge at the interior entrance.

The removal of two more residues in the deletion variants **S6E**/**S7D**/**S7G** converts the loop into a short linker, further widening the pore exterior entrance (Figure 4). The non-charged double glycine mutation of the **S7G** variant designed by *Williams et al.*[23] allows the pore-lining residues K195 and R196 to dominate the electrostatic profile, leading to a highly positive and concave pore opening and channel from the exterior viewpoint. On the interior surface, while E199 creates a negative ring around the interior opening, partially neutralized by the presence of K195. Comparing variants **S7G** and **S6E**, introduction of K185 and E193 in place of two glycines leads to a similar electrostatic profile, where K185 provides negative charge in addition to K149. In contrast, the introduction of D185 in variant **S7D** inverts the electrostatics of the exterior entrance while partially neutralizing the pore channel itself.

We note that in all deletion variants, the flexible side-chain of K195 is shown in a conformation that points into the pore in our structural models. As the HOLE program relies on the static structures provided, the calculated pore width at the interior entrance is not expected to be precise, especially for **S6E** where we anticipate a wider pore diameter after accounting for K195 side-chain flexibility.

To further investigate pore residue flexibility, we generated local resolution estimates for our final cryo-EM maps using cryoSPARC and an FSC gold-standard threshold of 0.143. It is well

established that a local decrease in resolution often correlates with increased local flexibility of loops and side chains.[43] Based on our analysis (SI Figure S6.3), all pore mutants display locally decreased resolutions between 0.3 and 0.5 Å in the residues surrounding the pore exterior. All loop deletion variants (**S5D**/**S6E**/**S7D**/**S7G**) and the triple point mutation variant **S3E** show a pronounced local decrease in resolution for all residues lining the interior of their wide pores including K195. On the other hand, the local resolution of the pore interior for the single point mutation variants **S1K** and **S1R** seems to represent a local resolution maximum. For **S1K** and **S1R**, residue Y191 represents the narrowest point of the pore and shows a local increase in resolution of ca. 0.5 Å indicating a locally rigid pore. Our local resolution analysis suggests that loop deletion and variants with increased negative charge density lead to generally more flexible pore residues.

Stopped-flow kinetics reveals the complexity of quantifying molecular flux into protein cages

To quantify the impact of pore variation on molecular influx, we used a lanthanide-based luminescence assay previously reported by *Williams et al.* for measuring the kinetics of ion influx into encapsulins (Figure 5a).[23] This assay involves genetically fusing a lanthanide binding tag (LBT) reported by Imperiali and co-workers to the *N*-terminus of the encapsulin gene,[40] thus resulting in 60 copies of the LBT displayed within the interior of every encapsulin protein cage. Upon binding to Tb^{3+}, energy transfer from a tryptophan in the LBT sequence to the lanthanide ion results in turn-on luminescence that can be measured using a stopped-flow apparatus and fitted to a one-phase association model. If the luminescent complex formation is extremely rapid, the rate constant of turn-on luminescence should reflect the kinetics of diffusion into the cage as the rate-determining step.

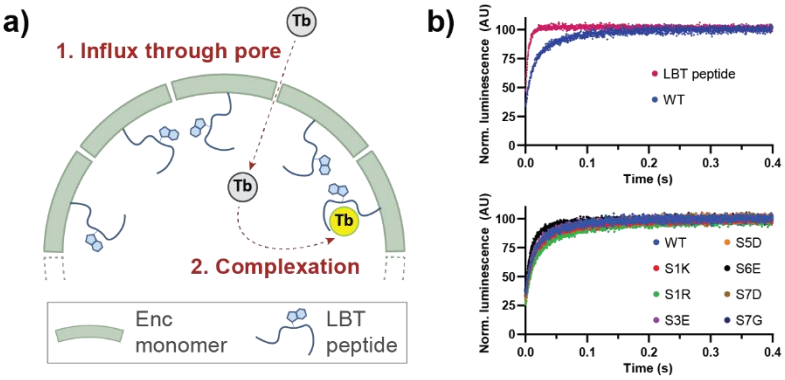

c)

Cage variant	Rate constant (s^{-1})
Free LBT peptide	180 ± 10
Wild-type (WT)	48 ± 3
S1K	50 ± 2
S1R	44 ± 2
S3E	55 ± 3
S5D	43 ± 2
S6E	70 ± 4
S7D	44 ± 2
S7G	46 ± 2

Figure 5: Quantifying kinetics of molecular flux into pore variants using a luminescence turn-on assay. a) Schematic of kinetic assay, where a lanthanide binding tag (LBT) peptide is internally fused to each copy of the encapsulin, such that luminescence turn-on mechanism involves Tb^{3+} diffusion through pores into the cage followed by complexation.[23,40] **b)** Top: Luminescence kinetic curves showing that the LBT peptide has a slower rate of turn-on when encapsulated. Bottom: Cage variants all show similar rates of luminescence turn-on. **c)** Table of pseudo-first order rate constants calculated from stopped-flow luminescence data.

We first measured the rapid kinetics of luminescence turn-on for the isolated LBT peptide that was obtained by solid-phase peptide synthesis. Maximal luminescence signal corresponding to equilibrated complexation of Tb^{3+} was reached in ~30 ms, giving a pseudo-first order rate constant of 180±10 s^{-1} (Figure 5b).

Next, we confirmed that the encapsulated LBT peptide had slower turn-on kinetics than the freely accessible peptide. Using a 70-fold excess of Tb^{3+}, wild-type encapsulin with internal *N*-terminally fused LBT gave a pseudo-first order rate constant of 48±3 s^{-1}, corresponding to approximately a four-fold reduction in rate constant compared to the free peptide (Figure 5b), qualitatively aligning with the general trend reported in the literature.[23] Upon comparing the turn-on kinetics of the seven pore variants with cryo-EM structures (Figure 5c), **S3E** and **S6E** showed slight increases over the wild-type rate with pseudo-first order rate constants of 55±3 s^{-1} and 70±4 s^{-1} respectively. There were minimal differences in rate for the remainder of the variants including the **S7G** control (46±2 s^{-1}), despite the significant differences in pore size and charge of all variants, in contrast with the literature.[23] Varying the initial Tb^{3+} concentration had no effect on the pseudo-first order rate constant for the free LBT peptide, while a non-linear dependence was observed for the wild-type and **S7G** encapsulated LBT peptides (SI Figure S7.4). This result indicates that the mechanistic processes governing luminescence turn-on are indeed different between free and encapsulated LBT peptide.

From the combined data, the reduction in turn-on kinetic rate upon encapsulation may therefore be representative of two mechanistic possibilities: restricted diffusion of Tb^{3+} through pores that is indeed similar across the range of variants, in contrast to the literature;[23] or alternatively, modified kinetics of Tb^{3+}-LBT complex formation due to genetic fusion and subsequent conformational changes in the LBT peptide within the encapsulin interior, such that the dominant rate-determining step is complex formation, rather than ion diffusion through the five-fold symmetric pore.

Discussion

In this study, we show that it is possible to build a library of protein cages featuring pores of different size and charge, showcasing the remarkable robustness of encapsulins and their tolerance to mutation, even when subjected to extended periods of high temperature. Our cryo-EM structures provide atomic-level understanding of how the designed sequence modifications translate to pore widening and charge inversion in the final cage assembly, enabling systematic structure-based design of nanoreactor porosity in future work.

Our discovery of the clear stability preference towards negatively charged pore mutations has significant broader implications for protein cage design. It may be possible to use this feature to control the integrity of cage assembly, as inducible destabilization of protein cages could be applied to the controlled release of encapsulated drug cargo, or switchable assembly of nanoreactors.[33] Furthermore, destabilization of capsids featuring pore arginine residues is a native feature of the HIV capsid, where polyanionic metabolites are required to induce stabilization of the overall assembly.[44–47] Our encapsulin variant library provides a robust and engineerable model for studying and mimicking the behavior of these complex biological systems.

Through our cryo-EM structures, we also discover that it is still possible to generate stable assemblies featuring negatively charged pores, without directly introducing new lysine or arginine residues at the pore. In particular, variants **S6E** and **S7G** both present positively charged pore exteriors which stem from changes in backbone alignment and the influence of more remote residues.

The lack of Tb^{3+} rate differences between the wild-type and most pore variants highlights the intrinsic complexity of designing and measuring flux into protein cages and nanoreactors in general. Naively, we would expect that the wide and negatively charged five-fold symmetric pore of **S5D** should enhance molecular flux in comparison to the narrow wild-type pore, yet we did not observe significant differences. We propose that fusion of the LBT peptide alters the binding kinetics in comparison to the free peptide, so that the measured turn-on rate does not reflect diffusion through the five-fold pore. The location of the *N*-terminus is almost directly under a different ~3 Å pore situated at the three-fold axis of symmetry, placing three LBT peptides in close proximity. This crowding may result in alternative binding conformations and intermediate complexation stoichiometries, or may preferentially bind ions that diffuse through the three-fold pore, which is not altered in this study. These findings imply that relative positioning of internal cargo and the resulting molecular crowding may have a major impact on nanoreactor kinetics and overall productivity.

The discrepancy between our findings and those of *Williams et al.*[23] (including control variant **S7G**) emphasizes the challenges when quantifying kinetics in encapsulated systems. As the kinetic assay conditions themselves were closely matched, differences may have arisen during sample purification. In our hands, we found that low-resolution SEC was insufficient to obtain a homogeneous sample. Non-specifically bound nucleic acids have been noted as a co-purified contaminant,[48] while we have also seen evidence of soluble but incorrectly assembled encapsulin aggregates from *E. coli* expression that can be removed with higher resolution SEC. Furthermore, we expect to observe ion transport behavior reminiscent of ion channels such as gramicidin A,[49] rather than simple Fickian diffusion as reported,[23] due to the relatively narrow protein pores with potential transient interaction sites for Tb^{3+}.[50] Indeed, there is evidence that iron transport behavior in ferritin cages is facilitated by the pore structure, involving charge-selective interactions and multiple coordination sites formed by the pore residues.[51–54]

With this library of protein cage variants in hand, future work will involve studying the impact of pore size and charge on encapsulated enzymes. We expect that enzymatic substrates, products, and co-factors, will all experience a greater diffusional barrier than a simple metal ion such as Tb^{3+}, slowing the molecular flux to an extent that they play an important role in the rate equation for the overall transformation. Furthermore, molecular dynamics simulations based on our cryo-EM structures should further enhance our understanding of how molecular flux changes in response to different pore structures, enabling the predictable design of nanoreactors with tailored selectivity and enhanced catalytic turnover for any chosen chemical reaction. Our work therefore represents a crucial step in the development of programmable large-scale and multiplexed nanoreactors for simultaneously conducting otherwise incompatible reactions inside live cells.

Experimental Methods

Molecular cloning

Codon optimized genes for the wild-type *T. maritima* encapsulin with and without an *N*-terminal lanthanide binding tag were commercially purchased as gBlocks (Integrated DNA Technologies) and cloned into pBAD-HisA vector using the BglII and HindIII restriction sites. The untagged variant plasmids were generated by whole-plasmid PCR with mutagenic primers (SI Table S2.1), using untagged wild-type *T. maritima* plasmid as a template followed by DpnI digestion and clean-up. Tagged pore mutant plasmids were constructed by Gibson assembly using NEBuilder HiFi DNA Assembly Master Mix (NEB) where the variant encapsulin genes and backbone were individually amplified by PCR. Chemically competent *E. coli* strain DH5α was used for all cloning procedures. Sequences of plasmids were confirmed by Sanger sequencing conducted through the Ramaciotti Centre for Genomics (UNSW, Australia). See associated GenBank files for full sequence details (Supplementary Data File S1).

Protein expression and purification

Designed encapsulin variants containing *N*-terminal lanthanide binding tags (SI Table S2.2) were expressed in BL21(DE3) cells. Overnight 5 mL cultures were diluted into 400 mL of fresh LB media and grown at 37 ºC until OD_{600} of 0.4 was reached. Expression was induced with 0.2% arabinose and the cells were incubated at 20 ºC overnight. Cells were then pelleted by centrifugation at 3900 rcf for 15 min and stored at -80 ºC.

Frozen cell pellets were resuspended in 24 mL of lysis buffer (20 mM Tris, 100 mM NaCl, 100 µg/mL DNase, 100 µg/mL lysozyme, pH 8) and incubated on ice for 10 min. Cells were lysed using a Sonopuls HD 4050 probe sonicator with a TS-106 probe (Bandelin) using an amplitude setting of 55% and a pulse time of 8 s on and 10 s off for a total time of 11 min. The lysate was clarified by centrifugation, then to the supernatant, NaCl was added to 250 mM and PEG-8000 to 10%(w/v) final concentration. The suspension was incubated on ice for 10 min then centrifuged. The supernatant was removed, and the pellet was dissolved in a total volume of 4 mL size exclusion buffer (20 mM Tris, 100 mM NaCl, pH 8).

The redissolved protein was subject to size exclusion chromatography using a Sephacryl S-500 16/60 column at a flow rate of 1 mL/min (SI Figure S3.2). Fractions containing encapsulin were identified by SDS-PAGE, pooled, and filtered to remove nucleic acids by ion exchange chromatography using a HiPrep Q XL 16/10 column at a flow rate of 5 mL/min (SI Figure S3.3). Flow-through fractions containing encapsulin were concentrated by ultrafiltration (Amicon 100 kDa MWCO) and subjected to two rounds of size exclusion chromatography with a Superose 6 10/300 GL column at a flow rate of 0.3 mL/min (SI Figure S3.4a). Protein concentrations were determined by absorbance at 280 nm. Purified proteins were stored in size exclusion buffer until further use.

Negative stain transmission electron microscopy (TEM)

Encapsulin samples for negative stain TEM were diluted to 100 µg/mL in 20 mM Tris pH 8. Gold grids (200-mesh coated with Formvar-carbon film, EMS) were made hydrophilic by glow discharge at 50 mA for 30 s. The grid was floated on 20 µL of sample for 1 min, blotted with filter paper, and washed once with distilled water before staining with 20 µL of uranyl acetate for 1 min. TEM images were captured using a JEOL-1400 at 120 keV at the Australian Centre for Microscopy and Microanalysis.

For TEM after DLS thermal stability experiments, samples were imaged with a Hitachi HT770 at 80 keV, using the same protocol except the grids were not glow discharged.

Size-exclusion chromatography with multi-angle light scattering (SEC-MALS)

SEC-MALS was performed using a Nexera Bio-HPLC (Shimadzu). Separations were performed using a Bio SEC-5 1000 Å 7.8 × 300 mm column (Agilent) with a Bio SEC-5 2000 Å 7.8 × 300 mm guard column (Agilent). Multi-angle light scattering was measured using a Dawn 8 Multi-Angle Light Scattering detector (Wyatt Technologies). Concentration was calculated from change in refractive index assuming a $\frac{dn}{dc}$ of 0.185. PBS was used as the mobile phase and kept at a constant flow rate of 1 mL/min. Samples for SEC-MALS analysis were typically diluted to 200 µg/mL and 25 µL was injected with a run time of 20 min. Molecular weights were calculated using ASTRA 7.3.0 software (Wyatt Technologies).

Dynamic light scattering (DLS)

The hydrodynamic size of encapsulin particles was determined using a Zetasizer Nano ZS (Malvern Analytical). DLS measurements were taken at 25 °C at a concentration of 17 µg/mL encapsulin in size exclusion buffer.

For thermal stability experiments, samples were loaded in duplicate on black glass-bottomed 384-well polystyrene plates (Corning) and overlayed with silicon oil (Sigma-Aldrich). Scheduled measurements were performed using a DynaPro III Plate Reader (Wyatt Technologies) and cumulants analysis was performed on 10 acquisitions per well by Dynamics V 7.9.1.4 (Wyatt Technologies).

Starting at 25 °C the temperature was increased by 2 °C each cycle (of approximately 30 minutes each) to 75 °C. Following the thermal gradient scan, a measurement was taken at 25 °C and this was followed by further overnight incubation at 80 °C, during which measurements were made every 30 minutes.

Cryo-electron microscopy (cryo-EM) sample preparation, data collection, and data processing

Grids for cryo-EM imaging of the five encapsulin variant samples **S1K**, **S1R**, **S3E**, **S6E** and **S7D** were prepared by applying 3.5 µL of purified encapsulin sample diluted in 150 mM NaCl,

25 mM Tris at pH 8.0 to a concentration of 2 mg/mL to a glow-discharged (1 min at 5 mA) holey carbon grid (Quantifoil Q225-CR1.3). This was followed by plunge-freezing in liquid ethane using an FEI Vitribot Mark IV (100% humidity, blot force: 20, wait time: 0, temperature: 22 °C). Grids were clipped and stored in liquid nitrogen until data collection.

Cryo-EM movies of samples **S1K**, **S1R**, **S3E**, **S6E** and **S7D** were collected at the University of Michigan Life Sciences Institute on a Glacios cryo-electron microscope (Thermo Fisher Scientific) operating at 200 kV and equipped with a K2 Summit direct electron detector (Gatan). Movies were collected at a magnification of 45,000 with a calibrated pixel size of 0.98 Å using the Leginon automated data collection software,[55,56] with an exposure time of 8 s and a frame time of 200 ms.

Grids for the two encapsulin variant samples **S5D** and **S7G** were prepared by applying 3 µL of purified encapsulin sample at a concentration of 2 mg/mL to holey carbon 2/2 C-flat grids. This was followed by plunge-freezing in liquid ethane using a FEI Vitribot Mark IV (95% humidity, blot force: 0, wait time: 30, temperature: 4 °C).

Cryo-EM movies of samples **S5D** and **S7G** were collected at University of New South Wales on an Arctica cryo-electron microscope (Thermo Fisher Scientific) operating at 200 kV equipped with a Falcon III EC detector. Movies were collected with a calibrated pixel size of 0.986 Å using Thermo Fisher EPU automated data collection software. The exposure time was 47.84 s with a 1.196 s frame time. Further details and parameters of cryo-EM data collection can be found in SI Tables S6.4 and S6.5.

All cryo-EM data processing was performed using cryoSPARC[57] v2.15.0. After importing movies, beam-induced and local motion was corrected using Patch motion correction. CTF correction was carried out using the Patch CTF estimation job. Then, 200 particles were manually picked using the Manual picker followed by 2D classification with 10 classes. Good classes were then used as templates for template-based particle picking via the Template picker. Picks were visually inspected to find optimal Local power and NCC score values. Particles were extracted with a box size of 384 pixels followed by two rounds of 2D classification using 100 and then 50 classes and otherwise standard parameters. Particle stacks were further cleaned via 3D classification using the Heterogeneous Refinement job with 3 classes, icosahedral symmetry (I) enforced and a refinement box size of 256 voxels. As initial models, volumes based on the X-ray structure of the *T. maritima* encapsulin (PDB ID: 3DKT) generated in UCSF Chimera 1.13.1rc were used. Particles of the largest 3D class were then used to carry out 3D refinement using the Homogeneous refinement (New) (I symmetry enforced, refinement box size: 384 voxels) job followed by Local and then Global CTF refinement with standard parameters. This was repeated 3× followed by a final round of 3D refinement. Local resolution estimation of final maps was done in cryoSPARC with the FSC threshold set to 0.143. Further details about cryo-EM data processing can be found in SI Tables S6.4 and S6.5 and SI Figures S6.1, S6.2 and S6.3.

Model building and refinement

Final cryoSPARC maps were opened in UCSF Chimera[58] version 1.14. An initial model was placed into the density by manually aligning a monomer of the *T. maritima* encapsulin (PDB ID: 3DKT) to the map, followed by the fit_to_volume command to improve the rigid body fit

into the density. Coordinates were then opened in Coot[59] version 0.9-pre and manually refined against the map. Briefly, the refinement strategy consisted of an initial rigid body refinement into the map, followed by chain refinement, and finally iterative manual real space refinements along the length of the protein. During refinement, density for a flavin-based molecule was identified between residues W87 and R78. Because the exact flavin derivative could not be identified from the density alone, riboflavin (RBF) was placed in the density and refined. Following manual refinements in Coot, coordinates were further refined as monomers in Phenix[60] version 1.18.2-3874 using phenix.real_space_refine with default parameters. Restraints for the riboflavin were generated using eLBOW[61] in Phenix. Non-crystallographic symmetry (NCS) was identified in the cryo-EM map via phenix.map_symmetry, and NCS operators were then applied using phenix.apply_ncs to construct a complete model with icosahedral symmetry. This model was then refined using phenix.real_space_refine with NCS restraints, global minimization, and ADP refinements. Models were then validated using the Comprehensive Validation (phenix.validation_cryoem) tool[62] in Phenix prior to submitting to the PDB. Models were assigned the following PDB identifiers: 7LII, 7LIJ, 7LIK, 7LIL, 7LIM, 7LIS, and 7LIT. Final cryo-EM maps were submitted to the EMDB with the following identifiers: 23379, 23380, 23381, 23382, 23383, 23384 and 23385.

Pore size measurements

The HOLE package (2.2.005) was used for measuring the radius of the 5-fold encapsulin pores.[41] The *T. maritima* encapsulin crystal structure 3DKT was used for measurements of the wild-type encapsulin,[28] while measurements of cage variants were based on cryo-EM structures. The default file was used to determine atomic Van der Waals radii. Measurements were conducted with a cut-off radius of 20 Å to analyse the interior and exterior surfaces of the pore in addition to the channel.

Synthesis and purification of LBT control peptide

Peptide synthesis was done on a Biotage Syro I Automated Parallel Peptide Synthesizer. Rink amide resin was treated with a solution of 40% piperidine in DMF (1.6 mL) for 4 min followed by a solution of 20% piperidine in DMF for 6 min. The resin was washed with DMF (4 × 2.5 mL). Fmoc-AA-OH (0.8 mL, 0.5 M), DIC (0.8 mL, 0.5 M), and Oxyma (0.8 mL, 0.55 M) were dispensed from stock solutions in DMF onto the resin. The reaction was heated to 75 °C and mixed for 15 min. Upon completion, the resin was washed with DMF (4 × 2.5 mL). For capping, the resin was treated with a solution of 2.5% acetic anhydride and 5% DIPEA in DMF (1.6 mL) for 6 min. The resin was then washed with DMF (4 × 2.5 mL).

Resin containing synthesised peptide was cleaved with a cocktail consisting of 90:5:5 TFA:water:triisopropylsilane with agitation for 1 h. The volume of the resulting peptide solution was reduced under a stream of nitrogen before being triturated with diethyl ether. The solid crude peptide was centrifuged, and the pellet was dissolved in 50:50 water:acetonitrile. The crude peptide solution was purified by reverse-phase HPLC (Sunfire C18 semi-prep 10 × 250 mm; Solvent A: water + 0.1% TFA; Solvent B: acetonitrile + 0.1% TFA) with a 0-100%

gradient over 20 min (peptide eluted at 14.1 min). Peptide fractions were combined and lyophilised to yield the pure LBT peptide (SI Section 5).

Stopped-flow kinetic assays

Stopped-flow kinetic assays for monitoring luminescence turn-on were performed using a KinetAsyst stopped-flow spectrophotometer (TgK Scientific). A Hg/Xe lamp was used for excitation at 282 nm, while all emission transmitted through a 455 nm longpass filter was integrated for data analysis.

Encapsulin samples for stopped-flow were buffer exchanged and prepared at a concentration of 7 µM in 100 mM HEPES-KOH, pH 7.6. $TbCl_3$ solutions were prepared at a concentration of 500 µM in 1 mM HCl, with solutions for each analysis made immediately prior to measurement by dilution from a 50 mM $TbCl_3$ stock solution in 1 mM HCl.

The temperature of the stopped-flow sample handling unit was set to 15 °C. Prior to each stopped-flow analysis, encapsulin and $TbCl_3$ solutions were equilibrated in the sample handling unit for 10 min prior to analysis.

Each measurement was performed by injecting 50 µL of each solution into the sample chamber and recording luminescence for 2 s (8192 data points, 48 oversampling, 0.03 ms time constant). Rate constants were determined by averaging at least seven independent measurements and fitting the curve to a first-degree exponential (one-phase association in Prism 8 GraphPad), using a fitting window of 7-90 ms for encapsulin samples, and 3-50 ms for the LBT peptide. The quoted errors are the upper bound for the 95% confidence interval based on the model fitting (SI Section 6).

Data availability

The sequence data, in GenBank format, for all the constructs created in this study are available in Supplementary Data File S1. All other data that support the findings of this study are available from the corresponding author upon request.

Acknowledgements

YHL acknowledges funding from the Australian Research Council (DE190100624) and the Westpac Foundation (WRF2020). TWG acknowledges support from the National Institutes of Health (R35GM133325). The authors acknowledge Assoc. Prof. Ronald Clarke for assistance with stopped-flow kinetics, Prof. Richard Payne for assistance with peptide synthesis, and Sydney Analytical for assistance with molecular characterization. Research reported in this publication was supported by the University of Michigan Cryo-EM Facility (U-M Cryo-EM). U-M Cryo-EM is grateful for support from the U-M Life Sciences Institute and the U-M Biosciences Initiative. The authors also acknowledge the facilities and the scientific and technical assistance of Microscopy Australia at the Australian Centre for Microscopy &

Microanalysis at the University of Sydney and the Electron Microscopy Unit at the University of New South Wales.

References

1. Greening, C. & Lithgow, T. Formation and function of bacterial organelles. *Nat. Rev. Microbiol.* **18**, 677–689 (2020).

2. Yeates, T. O., Kerfeld, C. A., Heinhorst, S., Cannon, G. C. & Shively, J. M. Protein-based organelles in bacteria: carboxysomes and related microcompartments. *Nat. Rev. Microbiol.* **6**, 681–691 (2008).

3. Price, G. D. & Badger, M. R. Evidence for the role of carboxysomes in the cyanobacterial CO 2 -concentrating mechanism. *Can. J. Bot.* **69**, 963–973 (1991).

4. Marcus, Y., Berry, J. & Pierce, J. Photosynthesis and photorespiration in a mutant of the cyanobacterium Synechocystis PCC 6803 lacking carboxysomes. *Planta* **187**, (1992).

5. Faulkner, M. *et al.* Molecular simulations unravel the molecular principles that mediate selective permeability of carboxysome shell protein. *Sci. Rep.* **10**, 17501 (2020).

6. Mahinthichaichan, P., Morris, D. M., Wang, Y., Jensen, G. J. & Tajkhorshid, E. Selective Permeability of Carboxysome Shell Pores to Anionic Molecules. *J. Phys. Chem. B* **122**, 9110–9118 (2018).

7. Dou, Z. *et al.* CO 2 Fixation Kinetics of Halothiobacillus neapolitanus Mutant Carboxysomes Lacking Carbonic Anhydrase Suggest the Shell Acts as a Diffusional Barrier for CO 2. *J. Biol. Chem.* **283**, 10377–10384 (2008).

8. Uchida, M. *et al.* Biological Containers: Protein Cages as Multifunctional Nanoplatforms. *Adv. Mater.* **19**, 1025–1042 (2007).

9. Azuma, Y., Edwardson, T. G. W. & Hilvert, D. Tailoring lumazine synthase assemblies for bionanotechnology. *Chem. Soc. Rev.* **47**, 3543–3557 (2018).

10. Kim, E. Y. & Tullman-Ercek, D. Engineering nanoscale protein compartments for synthetic organelles. *Curr. Opin. Biotechnol.* **24**, 627–632 (2013).

11. Lee, H., DeLoache, W. C. & Dueber, J. E. Spatial organization of enzymes for metabolic engineering. *Metab. Eng.* **14**, 242–251 (2012).

12. Lau, Y. H., Giessen, T. W., Altenburg, W. J. & Silver, P. A. Prokaryotic nanocompartments form synthetic organelles in a eukaryote. *Nat. Commun.* **9**, 1311 (2018).

13. Chen, A. H. & Silver, P. A. Designing biological compartmentalization. *Trends Cell Biol.* **22**, 662–670 (2012).

14. Giessen, T. W. & Silver, P. A. Encapsulation as a Strategy for the Design of Biological Compartmentalization. *J. Mol. Biol.* **428**, 916–927 (2016).

15. Cassidy-Amstutz, C. *et al.* Identification of a Minimal Peptide Tag for in Vivo and in Vitro Loading of Encapsulin. *Biochemistry* **55**, 3461–3468 (2016).

16. Choudhary, S., Quin, M. B., Sanders, M. A., Johnson, E. T. & Schmidt-Dannert, C. Engineered Protein Nano-Compartments for Targeted Enzyme Localization. *PLoS One* **7**, e33342 (2012).

17. Parsons, J. B. *et al.* Synthesis of Empty Bacterial Microcompartments, Directed Organelle Protein Incorporation, and Evidence of Filament-Associated Organelle Movement. *Mol. Cell* **38**, 305–315 (2010).

18. Rurup, W. F., Snijder, J., Koay, M. S. T., Heck, A. J. R. & Cornelissen, J. J. L. M. Self-Sorting of Foreign Proteins in a Bacterial Nanocompartment. *J. Am. Chem. Soc.* **136**, 3828–3832 (2014).

19. Patterson, D. P., Prevelige, P. E. & Douglas, T. Nanoreactors by Programmed Enzyme Encapsulation Inside the Capsid of the Bacteriophage P22. *ACS Nano* **6**, 5000–5009 (2012).

20. Hsia, Y. *et al.* Design of a hyperstable 60-subunit protein icosahedron. *Nature* **535**, 136–139 (2016).

21. Glasgow, J. E., Asensio, M. A., Jakobson, C. M., Francis, M. B. & Tullman-Ercek, D. Influence of Electrostatics on Small Molecule Flux through a Protein Nanoreactor. *ACS Synth. Biol.* **4**, 1011–1019 (2015).

22. Azuma, Y., Bader, D. L. V. & Hilvert, D. Substrate Sorting by a Supercharged Nanoreactor. *J. Am. Chem. Soc.* **140**, 860–863 (2018).

23. Williams, E. M., Jung, S. M., Coffman, J. L. & Lutz, S. Pore Engineering for Enhanced Mass Transport in Encapsulin Nanocompartments. *ACS Synth. Biol.* **7**, 2514–2517 (2018).

24. Slininger Lee, M. F., Jakobson, C. M. & Tullman-Ercek, D. Evidence for Improved Encapsulated Pathway Behavior in a Bacterial Microcompartment through Shell Protein Engineering. *ACS Synth. Biol.* **6**, 1880–1891 (2017).

25. Park, J., Chun, S., Bobik, T. A., Houk, K. N. & Yeates, T. O. Molecular Dynamics Simulations of Selective Metabolite Transport across the Propanediol Bacterial Microcompartment Shell. *J. Phys. Chem. B* **121**, 8149–8154 (2017).

26. Chowdhury, C. *et al.* Selective molecular transport through the protein shell of a bacterial microcompartment organelle. *Proc. Natl. Acad. Sci.* **112**, 2990–2995 (2015).

27. Chowdhury, C. & Bobik, T. A. Engineering the PduT shell protein to modify the permeability of the 1,2-propanediol microcompartment of Salmonella. *Microbiology* **165**, 1355–1364 (2019).

28. Sutter, M. *et al.* Structural basis of enzyme encapsulation into a bacterial nanocompartment. *Nat. Struct. Mol. Biol.* **15**, 939–947 (2008).

29. Rahmanpour, R. & Bugg, T. D. H. Assembly in vitro of Rhodococcus jostii RHA1 encapsulin and peroxidase DypB to form a nanocompartment. *FEBS J.* **280**, 2097–2104 (2013).

30. McHugh, C. A. *et al.* A virus capsid-like nanocompartment that stores iron and protects bacteria from oxidative stress. *EMBO J.* **33**, 1896–1911 (2014).

31. Giessen, T. W. *et al.* Large protein organelles form a new iron sequestration system with high storage capacity. *Elife* **8**, (2019).

32. Nichols, R. J., Cassidy-Amstutz, C., Chaijarasphong, T. & Savage, D. F. Encapsulins: molecular biology of the shell. *Crit. Rev. Biochem. Mol. Biol.* **52**, 583–594 (2017).

33. Giessen, T. W. Encapsulins: microbial nanocompartments with applications in biomedicine, nanobiotechnology and materials science. *Curr. Opin. Chem. Biol.* **34**, 1–10 (2016).

34. Jones, J. A. & Giessen, T. W. Advances in encapsulin nanocompartment biology and engineering. *Biotechnol. Bioeng.* **118**, 491–505 (2021).

35. Kanekiyo, M. *et al.* Rational Design of an Epstein-Barr Virus Vaccine Targeting the Receptor-Binding Site. *Cell* **162**, 1090–1100 (2015).

36. Choi, B. *et al.* Effective Delivery of Antigen–Encapsulin Nanoparticle Fusions to Dendritic Cells Leads to Antigen-Specific Cytotoxic T Cell Activation and Tumor Rejection. *ACS Nano* **10**, 7339–7350 (2016).

37. Putri, R. M. *et al.* Structural Characterization of Native and Modified Encapsulins as Nanoplatforms for in Vitro Catalysis and Cellular Uptake. *ACS Nano* **11**, 12796–12804 (2017).

38. Sigmund, F. *et al.* Bacterial encapsulins as orthogonal compartments for mammalian cell engineering. *Nat. Commun.* **9**, 1990 (2018).

39. Giessen, T. W. & Silver, P. A. Converting a Natural Protein Compartment into a Nanofactory for the Size-Constrained Synthesis of Antimicrobial Silver Nanoparticles. *ACS Synth. Biol.* **5**, 1497–1504 (2016).

40. Franz, K. J., Nitz, M. & Imperiali, B. Lanthanide-Binding Tags as Versatile Protein Coexpression Probes. *ChemBioChem* **4**, 265–271 (2003).

41. Smart, O. S., Goodfellow, J. M. & Wallace, B. A. The pore dimensions of gramicidin A. *Biophys. J.* **65**, 2455–2460 (1993).

42. Jurrus, E. *et al.* Improvements to the APBS biomolecular solvation software suite. *Protein Sci.* **27**, 112–128 (2018).

43. Vilas, J. *et al.* Local resolution estimates of cryoEM reconstructions. *Curr. Opin. Struct. Biol.* **64**, 74–78 (2020).

44. Yu, A., Lee, E. M. Y., Jin, J. & Voth, G. A. Atomic-scale characterization of mature HIV-1 capsid stabilization by inositol hexakisphosphate (IP 6). *Sci. Adv.* **6**, eabc6465 (2020).

45. Mallery, D. L. *et al.* IP6 is an HIV pocket factor that prevents capsid collapse and promotes DNA synthesis. *Elife* **7**, (2018).

46. Jacques, D. A. *et al.* HIV-1 uses dynamic capsid pores to import nucleotides and fuel encapsidated DNA synthesis. *Nature* **536**, 349–353 (2016).

47. Neves, M. A. C., Yeager, M. & Abagyan, R. Unusual Arginine Formations in Protein Function and Assembly: Rings, Strings, and Stacks. *J. Phys. Chem. B* **116**, 7006–7013 (2012).

48. Moon, H., Lee, J., Min, J. & Kang, S. Developing Genetically Engineered Encapsulin Protein Cage Nanoparticles as a Targeted Delivery Nanoplatform. *Biomacromolecules* **15**, 3794–3801 (2014).

49. Andrew Woolley, G. & Wallace, B. A. Model ion channels: Gramicidin and

alamethicin. *J. Membr. Biol.* **129**, (1992).

50. Chung, S.-H. & Kuyucak, S. Recent advances in ion channel research. *Biochim. Biophys. Acta - Biomembr.* **1565**, 267–286 (2002).

51. Laghaei, R., Kowallis, W., Evans, D. G. & Coalson, R. D. Calculation of iron transport through human H-chain ferritin. *J. Phys. Chem. A* **118**, 7442–53 (2014).

52. Tosha, T., Ng, H.-L., Bhattasali, O., Alber, T. & Theil, E. C. Moving metal ions through ferritin-protein nanocages from three-fold pores to catalytic sites. *J. Am. Chem. Soc.* **132**, 14562–9 (2010).

53. Yang, X., Arosio, P. & Chasteen, N. D. Molecular diffusion into ferritin: pathways, temperature dependence, incubation time, and concentration effects. *Biophys. J.* **78**, 2049–59 (2000).

54. Laghaei, R., Evans, D. G. & Coalson, R. D. Metal binding sites of human H-chain ferritin and iron transport mechanism to the ferroxidase sites: a molecular dynamics simulation study. *Proteins* **81**, 1042–50 (2013).

55. Suloway, C. *et al.* Automated molecular microscopy: The new Leginon system. *J. Struct. Biol.* **151**, 41–60 (2005).

56. Carragher, B. *et al.* Leginon: An Automated System for Acquisition of Images from Vitreous Ice Specimens. *J. Struct. Biol.* **132**, 33–45 (2000).

57. Punjani, A., Rubinstein, J. L., Fleet, D. J. & Brubaker, M. A. cryoSPARC: algorithms for rapid unsupervised cryo-EM structure determination. *Nat. Methods* **14**, 290–296 (2017).

58. Pettersen, E. F. *et al.* UCSF Chimera--a visualization system for exploratory research and analysis. *J. Comput. Chem.* **25**, 1605–12 (2004).

59. Emsley, P., Lohkamp, B., Scott, W. G. & Cowtan, K. Features and development of Coot. *Acta Crystallogr. D. Biol. Crystallogr.* **66**, 486–501 (2010).

60. Liebschner, D. *et al.* Macromolecular structure determination using X-rays, neutrons and electrons: recent developments in Phenix. *Acta Crystallogr. Sect. D, Struct. Biol.* **75**, 861–877 (2019).

61. Moriarty, N. W., Grosse-Kunstleve, R. W. & Adams, P. D. electronic Ligand Builder and Optimization Workbench (eLBOW): a tool for ligand coordinate and restraint generation. *Acta Crystallogr. D. Biol. Crystallogr.* **65**, 1074–80 (2009).

62. Williams, C. J. *et al.* MolProbity: More and better reference data for improved all-atom structure validation. *Protein Sci.* **27**, 293–315 (2018).